JTSES
Journal of Thermal and Sustainable Energy Systems

https://jtses.com/index.php/home/index

Contamination-Controlled Recycle of Inconel 718 Swarf through Y_2O_3-HfO_2 Dispersion Engineering and Spark Plasma Sintering

Sivaramkumar Sampathkumar [1]*, Sujitha Lakshmanan [2], V. Ellappan [3], R. Karikalan [4]

[1] Department of Mechanical Engineering, Paavai College of Engineering, Namakkal – 637018, Tamil Nadu, India — Email: er.sivaramkumar@gmail.com

[2] Department of Electronics and Communication Engineering, Paavai Engineering College, Namakkal – 637018, Tamil Nadu, India — Email: sujitha090593@gmail.com

[3] Department of Electronics and Communication Engineering, Mahendra Institute of Technology (Autonomous), Tiruchengode, Namakkal – 637503, Tamil Nadu, India — Email: ellappan.v@gmail.com

[4] Department of Mechatronics Engineering, Mahendra Engineering College (Autonomous), Namakkal – 637503, Tamil Nadu, India — Email: karikalan.r.k@gmail.com

Corresponding Author*: Sivaramkumar Sampathkumar — Email: er.sivaramkumar@gmail.com

ABSTRACT

Machining swarf from Inconel 718 retains valuable nickel, chromium, and niobium, yet conventional remelting increases energy demand and risks oxidation and compositional loss. Direct solid-state recycle offers a route that combines critical-metal recovery with oxide-dispersion strengthening. Existing routes have not integrated contamination-controlled swarf, deliberate Y_2O_3-HfO_2 dispersion engineering, pressure-assisted consolidation, and material-genealogy-based oxygen accounting. This investigation aims to establish relationships among swarf contamination, oxide chemistry, spark-plasma-sintering response, and high-temperature performance in recycled ODS-IN718. Swarf was cleaned, fragmented, mechanically alloyed with controlled oxide additions, consolidated by spark plasma sintering, heat treated, and assessed using chemical analysis, X-ray diffraction, electron microscopy, and mechanical characterization. Stoichiometric calculations separated intentional oxide-derived oxygen from processing-derived excess oxygen. Y_2O_3 additions produced intentional oxygen concentrations of 638, 1063, and 1488 ppm, while combined Y_2O_3-HfO_2 formulations yielded 1215 and 1443 ppm. These calculations established that total oxygen alone could not represent contamination in oxide-containing material. The genealogy framework also distinguished recycled, virgin-powder, and wrought conditions without assigning unsupported experimental performance values. This recycle strategy supports circular superalloy manufacturing, resource efficiency, and chemically defensible assessment of ODS feedstocks. Future research should validate the processing window through independent industrial swarf streams, long-duration creep, cyclic oxidation, fatigue, and nanoscale dispersoid-stability measurements.

KEYWORDS: IN718 swarf recycle, oxide-dispersion strengthening, Y_2O_3-HfO_2 dispersoids, mechanical alloying, spark plasma sintering

INTRODUCTION

Inconel 718 (IN718) has remained one of the most widely deployed precipitation-hardened Ni–Fe–Cr superalloys because its γ matrix can be strengthened by coherent γ′ and γ″ precipitates while retaining useful oxidation resistance, fatigue resistance, and manufacturability at intermediate-to-high temperatures. The same alloy, however, has remained difficult to machine because of its high hot hardness, work-hardening tendency, and low thermal conductivity, and substantial quantities of high-value machining swarf have consequently been generated during component manufacture. Direct recovery of that waste has attracted increasing attention because conventional recycling through remelting, refining, and re-atomisation has introduced additional energy demand and has partially removed the environmental advantage of material recovery. Ball-milling-based conversion of machining waste into powder has already been proposed as a lower-energy route, although particle morphology, contamination, and powder flowability have remained important constraints (Dhiman et al., 2021). Multi-stage milling of Ti6Al4V swarf further demonstrated that controlled comminution could produce powder suitable for additive manufacturing while consuming substantially less energy than gas atomisation (Dhiman et al., 2022).

More recently, IN718 cutting chips were directly converted into regenerated powder by ball milling and successfully used for laser cladding, although irregular morphology and lower packing density produced measurable differences from gas-atomised powder (Zhang et al., 2026). These observations established the feasibility of direct chip-to-powder conversion, but they also showed that successful recycling depended on contamination control and subsequent consolidation rather than particle-size refinement alone.

Powder reuse studies on IN718 provided a second body of evidence relevant to swarf-derived feedstock. Repeated LPBF reuse changed particle size and flow characteristics without markedly degrading tensile properties over fourteen reuse cycles (Yi et al., 2021). After fifty reuse cycles, only modest changes in the as-built microstructure and mechanical behaviour were detected, although oxygen content in the reused powder rose substantially (Paccou et al., 2021). Reused IN718 powder also produced only marginal changes in fracture toughness and fatigue-crack propagation at 25 and 650 °C (Choi et al., 2021). In contrast, detailed tensile, compression, and creep testing showed that powder history could alter dislocation density, dispersion hardening, serrated yielding, and temperature-dependent creep response even when bulk grain structure remained similar (Bhowmik et al., 2022). Powder oxidation during reuse could itself generate fine alumina dispersions that delayed recrystallisation and modified tensile behaviour, demonstrating that oxygen could act either as contamination or as a strengthening precursor depending on its chemical state and spatial distribution (Lee et al., 2022). Secondary-source IN718 produced by scrap atomisation also achieved static and fatigue properties comparable with conventional feedstock while substantially lowering life-cycle energy and carbon burdens (Benedetti et al., 2024). The evidence therefore indicated that recycled origin alone did not determine performance; instead, oxygen uptake, oxide chemistry, morphology, and downstream thermomechanical processing controlled whether recycling remained benign or became detrimental.

Against this background, oxide-dispersion strengthening provided a technically attractive route for deliberately converting controlled oxygen-bearing additions into stable nanoscale strengthening populations. Mechanical alloying of a Ni–20Cr–20Fe–0.6Y_2O_3 composition showed progressive Fe and Cr dissolution, refinement of yttria, and preservation of nanoscale structure during subsequent thermal exposure (Gaikwad et al., 2024a). Elemental IN718 powders similarly required extended high-energy milling before a complete γ solid solution was produced, while cold welding, fracture, and dynamic recrystallisation evolved continuously with milling time (Ajay et al., 2024). Direct powder forging of mechanically alloyed Ni–Cr–Fe feedstock subsequently generated near-full density, ultrafine equiaxed grains, and limited prior-particle-boundary networks (Gaikwad et al., 2024b). An analogous Y_2O_3-containing Ni-based ODS alloy reached greater than 99% density with approximately 503 nm grains and a uniformly dispersed nanoscale oxide population after powder forging (Gaikwad et al., 2024c). These studies established a clear processing sequence in which mechanical alloying generated chemical homogeneity, structural refinement, and dispersoid redistribution, whereas rapid pressure-assisted consolidation determined porosity removal and interparticle bonding.

The Table 1 shows that the principal design variables were not independent. Milling route altered dispersoid distribution; oxide content altered precipitation and ductility; Hf or Zr modified oxide chemistry; SPS temperature controlled density and grain evolution; and heat treatment redistributed the γ′/γ″ contribution. A direct swarf-to-ODS route therefore required simultaneous control of feedstock cleanliness, oxide balance, milling severity, consolidation, Table 1:**studies defining processing–microstructure–property relationships relevant to recycled and ODS-strengthened IN718.**

Reference/Citation	Objective/Aim	Methodology/Approach	Materials/Parameters Studied	Key Findings/Results	Relevance to Current Study
Gaikwad et al. (2025a)	Compare yttria incorporation routes	Milling, cryomilling, forging, ageing	IN718 + 0.3 wt% Y_2O_3	△ Cryomilling promoted finer intragranular	Guides oxide-mixing route selection

Reference/Citation	Objective/Aim	Methodology/Approach	Materials/Parameters Studied	Key Findings/Results	Relevance to Current Study
				oxide dispersion	
Gaikwad et al. (2025b)	Assess powder-forged IN718 at temperature	Powder forging, TEM, tensile testing	IN718; room to elevated temperature	△ Near-full density supported near-isotropic mechanical response	Provides non-ODS solid-state benchmark
Gaikwad et al. (2025c)	Resolve yttria-dependent hot deformation	Cryomilling, forging, ageing, tensile tests	0.3–1 wt% Y_2O_3; 650 °C	△ Dispersoids and precipitates jointly controlled strengthening	Supports combined strengthening interpretation
Gaikwad et al. (2026)	Quantify ODS oxidation response	Forging, ageing, 850 °C oxidation	IN718; 0.7 wt% Y_2O_3	▽ ODS scale remained below 1.5 µm	Establishes oxidation-performance benchmark
Ma et al. (2024)	Determine SPS densification mechanisms	SPS, tensile, compression, microscopy	Temperature and heating-rate variations	△ Pulse current accelerated densification and grain strengthening	Defines SPS process sensitivity
Yalcin et al. (2022)	Design additively manufactured ODS-IN718	CALPHAD, ball milling, SLM, heat treatment	IN718 + 0.3 wt% Y_2O_3	△ Y–Ti–O oxides accompanied >99% density	Supports thermodynamic oxide design
Yu et al. (2022)	Evaluate Zr/Hf oxide modification	MA, HIP, TEM, tensile testing	Y_2O_3 with Zr and Hf	△ Hf-containing oxides became finer and denser	Justifies HfO_2 screening
Yu et al. (2023a)	Isolate Hf influence	High-energy milling, HIP, tensile testing	Low-Al Ni ODS; Hf addition	△ Hf refined oxides to approximately 13 nm	Defines Hf refinement mechanism
He et al. (2024)	Compare oxide-forming additions	MA, HIP, HRTEM, tensile testing	Y, La, Ce oxide precursors	△ Nano-oxide chemistry governed strengthening contributions	Supports chemistry-resolved TEM analysis

Reference/Citation	Objective/Aim	Methodology/Approach	Materials/Parameters Studied	Key Findings/Results	Relevance to Current Study
Yang et al. (2025)	Quantify nanoparticle strengthening	Powder modification, PBF, microscopy, tensile	IN718 + Y_2O_3 nanoparticles	△ Grain, carbide, dislocation strengthening acted synergistically	Demonstrates multi-mechanism ODS response

The dominant experimental approaches combined high-energy mechanical alloying or cryomilling with HIP, powder forging, SPS, or laser-based consolidation, followed by SEM, EBSD, TEM, and mechanical testing. Across these routes, finer and more uniformly distributed oxides generally coincided with stronger grain-boundary pinning and higher strength, whereas excessive oxide content promoted agglomeration or ductility penalties. Hf- and Zr-bearing systems differed from simple Y_2O_3 additions because complex Y–Hf–O and Y–Zr–O phases altered dispersoid size and spacing rather than merely adding oxide volume. SPS studies further showed that densification and strengthening were highly sensitive to temperature and heating conditions. Powder-recycling studies differed fundamentally from deliberate ODS processing because their oxygen-bearing particles originated through repeated handling and exposure rather than controlled oxide addition.

The field therefore progressed from demonstrating that IN718 powder could be reused or produced from secondary feedstock toward deliberately engineering recycled or powder-metallurgy feedstocks through oxide dispersion, grain refinement, and rapid consolidation. Sustainable IN718 blade manufacture using mixed recycled and virgin powder preserved room- and elevated-temperature properties while reducing raw-material demand (Liu et al., 2025). Direct ODS-IN718 development by thermochemical design confirmed that Y-containing nano-oxides could be integrated with conventional γ'/γ'' precipitation strengthening (Yalcin et al., 2022). Hf addition refined nanoscale oxides and changed their phase constitution in Ni-based ODS alloys (Yu et al., 2023a). Al content independently changed both oxide chemistry and γ' precipitation, demonstrating strong coupling between dispersoid design and precipitation strengthening (Yu et al., 2023b). LPBF-produced NiCrFeY alloys further showed that nanoscale Y_2O_3 could pin dislocations and remain effective at elevated temperature (Xu et al., 2022). Y addition in a laser-processed Ni superalloy similarly stabilised dislocation structures during high-temperature deformation (Wang et al., 2022). Bimodal-grained ODS Ni alloys demonstrated that dispersion strengthening and grain-size design could be balanced to mitigate the usual strength–ductility trade-off (He et al., 2021). Recent Y_2O_3-modified IN718 produced by powder-bed fusion showed simultaneous grain, carbide, dislocation, and precipitation strengthening (Yang et al., 2025). Similar MA–SPS processing of a Ni-rich ODS alloy showed that excessive oxide loading could impair densification through agglomeration despite strengthening at intermediate additions (Sabat et al., 2025). More broadly, degradation studies of recycled metallic powders established that powder history must be evaluated through chemistry, morphology, and component-level validation rather than reuse count alone (Powell et al., 2020).

Existing studies nevertheless left several coupled limitations unresolved. Direct chip-to-powder work established mechanical regeneration but did not integrate contamination genealogy, deliberate ODS chemistry, and bulk solid-state consolidation within one IN718 route (Zhang et al., 2026). Powder-reuse studies quantified oxygen accumulation but generally treated oxygen as a reuse-induced variable rather than separating uncontrolled oxygen pickup from stoichiometric oxygen intentionally introduced through Y_2O_3 or HfO_2 (Paccou et al., 2021) (Lee et al., 2022). ODS-IN718 studies investigated selected yttria contents or consolidation routes but used virgin or pre-alloyed powders rather than compositionally traceable machining swarf (Gaikwad et al., 2025a) (Yalcin et al., 2022). Hf-bearing ODS studies demonstrated oxide refinement but did not couple Hf chemistry with recycled IN718 contamination and SPS processing (Yu et al., 2022) (Yu et al., 2023a). SPS investigations focused on restricted temperature and heating-rate domains, while powder-forging studies used different stress states and

densification histories, limiting direct comparison across consolidation routes (Ma et al., 2024) (Gaikwad et al., 2025b). Consequently, contaminant evolution, nanoscale oxide chemistry, densification, precipitation, and high-temperature performance were rarely evaluated as a single connected process chain, and validation against wrought, virgin-powder, and recycled non-ODS controls remained insufficient for establishing scalable processing windows.

The present study differentiated the processing route by using compositionally traceable IN718 machining swarf as the direct alloy feedstock, applying staged decontamination and genealogy-based interstitial tracking before mechanical alloying, and separating recycled non-ODS material from Y_2O_3- and Y_2O_3–HfO_2-modified conditions. Milling and SPS parameters were evaluated within structured multivariable designs, while total oxygen was partitioned into intentional oxide-derived oxygen and process-derived excess oxygen. The resulting billets were compared with wrought and virgin-powder controls through density, SEM, EBSD, XRD, TEM/STEM, and complementary nanoscale chemical analysis, and the microstructural descriptors were linked directly to room-temperature and elevated-temperature tensile behaviour, creep response, and oxidation resistance.

The objective of the present study is to establish the relationships among contamination-controlled IN718 swarf recycling, Y_2O_3–HfO_2 mechanical alloying, SPS densification, nanoscale oxide evolution, precipitation behaviour, and high-temperature performance during direct solid-state production of ODS-IN718.

2. Materials and Methods

2.1. Experimental strategy and material genealogy

A contamination-controlled solid-state processing route was used to convert Inconel 718 (IN718) machining swarf into bulk oxide-dispersion-strengthened (ODS) material without remelting or re-atomisation. The experimental sequence comprised feedstock qualification, swarf sorting and decontamination, controlled mechanical fragmentation, mechanical alloying with nanoscale Y_2O_3 and HfO_2, powder characterisation, spark-plasma sintering (SPS), post-consolidation heat treatment, microstructural analysis, and mechanical and environmental evaluation. Particular emphasis was placed on tracing oxygen, carbon, nitrogen, hydrogen, and machining-derived contaminants through the processing sequence because the scientific objective required deliberate oxide additions to be distinguished from uncontrolled contamination. The processing concept followed the direct swarf-to-ODS route originally defined for the study.

Four principal material groups were evaluated. Wrought IN718 was used as the conventional reference material. Virgin pre-alloyed IN718 powder was subjected to comparable milling and consolidation conditions to identify effects caused by powder-processing history. Cleaned swarf-derived IN718 processed without deliberate oxide addition was used as the recycled non-ODS control. Cleaned swarf-derived IN718 containing Y_2O_3 or combined Y_2O_3–HfO_2 additions constituted the experimental ODS groups. Where available, remelted or re-atomised recycled IN718 was included as an additional recycling-route benchmark. This control architecture was adopted because mechanical milling of IN718 machining chips, Y_2O_3-containing ODS-IN718, and SPS processing of IN718 had already been demonstrated independently, whereas the principal research question concerned their integration within a contamination-controlled, no-remelt swarf-upcycling route.

Each material was assigned a hierarchical identification code linking the parent alloy, swarf collection, cleaning batch, milling batch, oxide formulation, SPS billet, heat-treatment condition, and final test specimen. Measurements made at several positions within one billet were treated as nested technical observations rather than independent processing replicates. Independent powder batches and independently consolidated SPS billets were therefore preserved as the principal experimental units.

The complete experimental route and relationship between the control and ODS processing streams are illustrated schematically in Figure 1.

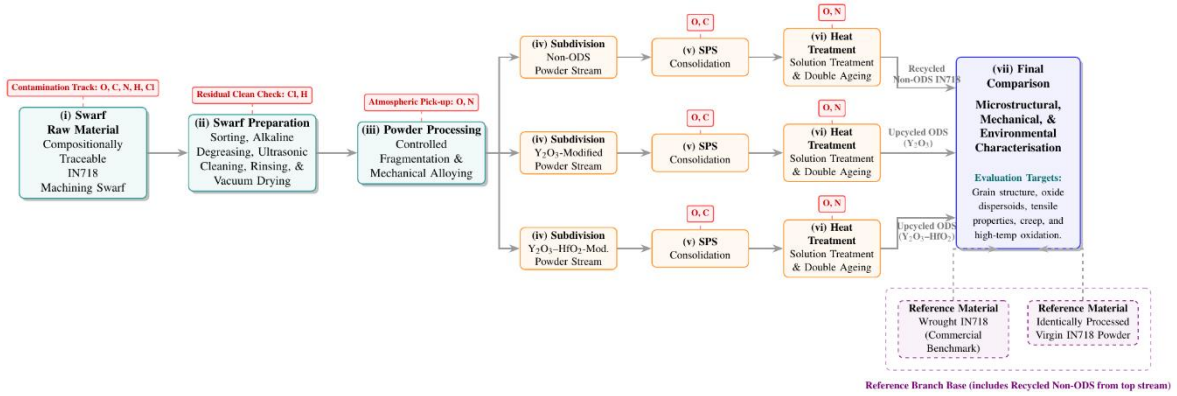

Figure 1:. **Schematic workflow for the direct solid-state upcycling of IN718 machining swarf into ODS-IN718.**

The major variables and responses used during process development are summarised in Table 1.

Table 2: **Experimental variables, processing conditions, and principal response parameters used during solid-state processing of swarf-derived IN718.**

Processing stage	Variable	Experimental conditions	Principal responses
Feedstock qualification	Swarf condition	Dry-machined, coolant-exposed, and independent industrial swarf	Composition, morphology, O, C, N, H, S, Cl
Cleaning	Cleaning route	As-received; alkaline-ultrasonic; enhanced pre-degreasing plus alkaline-ultrasonic	Mass recovery, residual C, S and Cl
Mechanical alloying	Milling time	4, 10 and 16 h	Particle size, morphology, strain, contamination
	Ball-to-powder ratio	5:1, 10:1 and 15:1	Fragmentation efficiency, recovery, contamination
	Milling intensity	Low, intermediate and high machine-equivalent conditions	Particle refinement, cold welding, contamination
Oxide formulation	Y_2O_3 content	0, 0.3, 0.5 and 0.7 wt%	Oxide distribution, microstructure, properties
	Y_2O_3–HfO_2	0.5 + 0.10 and 0.5 + 0.25 wt%	Oxide chemistry and thermal stability
SPS	Temperature	1050, 1125 and 1200 °C	Density, porosity, grain size, phases
	Pressure	30, 50 and 70 MPa	Densification and microstructure
	Holding time	5, 10 and 15 min	Densification, grain growth, contamination

Processing stage	Variable	Experimental conditions	Principal responses
Heat treatment	Thermal condition	As-SPS; direct aged; 980 °C solution + aged; 1050 °C solution + aged	γ′/γ″/δ/Laves evolution
Mechanical testing	Temperature	Ambient and 650 °C	Yield strength, UTS, ductility
Environmental testing	Exposure	Creep and 850 °C oxidation	Creep response, mass change and oxide-scale structure

2.2. IN718 feedstock and machining-swarf collection

Compositionally traceable IN718 was used as the principal feedstock so that variations introduced during recycling could be distinguished from variations already present in the parent alloy. The parent material was chemically qualified before machining, and the concentrations of Ni, Cr, Fe, Nb, Mo, Ti, Al, and other relevant alloying elements were established together with the principal interstitial and residual elements.

Machining swarf was collected under controlled conditions. A comparatively clean fraction was generated under dry-machining conditions, whereas a second fraction was collected following machining with water-based cutting fluid. The coolant-exposed material was included to represent the contamination encountered during practical industrial machining rather than restricting the investigation to artificially clean chips. An independently sourced swarf batch was also preserved for evaluation of process transferability after the principal processing window had been established.

The collected swarf was mechanically sorted according to source and gross chip morphology. Foreign metallic fragments and visibly dissimilar debris were removed before cleaning. Representative portions of each swarf batch were preserved in the as-generated state to provide baseline material for subsequent chemical and morphological comparisons.

Initial chip morphology was examined by scanning electron microscopy (SEM). Bulk alloy chemistry and the concentrations of O, C, N, H, S, and Cl were determined because these species could have originated from surface oxidation, machining lubricants, cleaning residues, environmental storage, milling, or consolidation. These initial measurements established the first two stages of the material genealogy: the parent alloy, designated P0, and the as-generated swarf, designated P1.

2.3. Swarf decontamination and cleaning validation

Gross particulate matter was first removed from the swarf by mechanical sorting. The material was subsequently immersed in an aqueous alkaline cleaning solution containing approximately 2–5 wt% alkaline detergent and was maintained at 50–60 °C. Ultrasonic agitation was applied for 15–30 min to assist disruption and removal of adherent oil, coolant residues, and particulate films present within folded and irregular chip surfaces.

Following alkaline treatment, the swarf was rinsed repeatedly with de-ionised water. An alcohol displacement rinse was subsequently applied to accelerate removal of residual water, after which the material was vacuum dried at moderate temperature. A more intensive cleaning route was additionally applied to heavily contaminated coolant-exposed swarf. In this route, compatible non-chlorinated pre-degreasing was performed before alkaline-ultrasonic treatment. Chlorinated organic cleaning agents were excluded to minimise the possibility of introducing chloride contamination.

Cleaning performance was evaluated from both mass and chemical balances. Dry swarf mass was determined before and after treatment, and metallic recovery was calculated as

$$Y_{clean} = \frac{m_{clean}}{m_{initial}} \times 100, \qquad (1)$$

where Y_{clean}represented cleaning-stage metal recovery, m_{clean}represented the dry mass after cleaning, and $m_{initial}$represented the corresponding initial swarf mass.

Carbon, sulfur, chlorine, oxygen, and nitrogen concentrations were measured before and after cleaning. Representative swarf surfaces were examined by SEM and energy-dispersive X-ray spectroscopy (EDS) to assess the persistence of adherent residues. Major metallic constituents were also compared before and after treatment to ensure that the cleaning procedure had not produced appreciable preferential dissolution or compositional alteration.

The cleaned material constituted genealogy point P2. Only batches in which reproducible contaminant removal had been obtained without significant metallic-element loss were advanced to mechanical processing.

2.4. Mechanical fragmentation and mechanical alloying

The cleaned and dried swarf was mechanically pre-fragmented before high-energy milling. Direct mechanical fragmentation constituted the primary powder-production route because preservation of a no-remelt processing pathway formed an essential part of the experimental design. Particle-size reduction therefore proceeded through repeated deformation, fracture, cold welding, and re-fracture during milling.

Hydrogen-assisted fragmentation was evaluated only as a separately controlled processing option rather than as an unavoidable stage of the recycling route. Direct mechanical fragmentation was preferentially applied because milling of IN718 machining chips had already been shown to provide a viable pathway for converting chips into powder. Where hydrogen-assisted embrittlement was applied, subsequent dehydrogenation was performed and residual hydrogen was measured before consolidation. Hydrogen-treated powder was not incorporated into the principal ODS route unless residual hydrogen had returned to the validated baseline range.

Mechanical alloying was performed in sealed milling vessels under an inert atmosphere. Vessel loading and powder handling were conducted under low-moisture and low-oxygen conditions where the equipment configuration permitted. Carbon-containing process-control agents were excluded from the principal milling route because uncontrolled carbon addition would have complicated interpretation of the contamination balance and could have promoted additional carbide formation.

Milling times of 4, 10, and 16 h were investigated in combination with ball-to-powder ratios of 5:1, 10:1, and 15:1. Three machine-equivalent milling intensities spanning low, intermediate, and high energy levels were evaluated. These conditions corresponded approximately to rotational settings of 300, 450, and 600 rpm where a rotational-speed description was applicable to the milling system. A response-surface or D-optimal experimental arrangement was used rather than a complete factorial combination so that interaction and curvature effects could be assessed without producing an unnecessarily large number of powder batches.

Potential contamination from milling media was examined before the principal milling programme. Short-duration trials were performed with candidate media, and resulting powders were analysed for Fe, Cr, W, Co, and C. The milling configuration that provided satisfactory fragmentation with the lowest detectable foreign-element pickup was used for the principal experiments.

Powder recovery after milling was calculated as

$$Y_{powder} = \frac{m_{usable\ powder}}{m_{clean\ swarf}} \times 100, \qquad (2)$$

where $m_{usable\ powder}$represented the mass of recovered powder suitable for subsequent processing and $m_{clean\ swarf}$represented the cleaned swarf mass introduced into the milling operation.

The experimentally controlled powder-processing branches and corresponding reference conditions are shown in Figure 2.

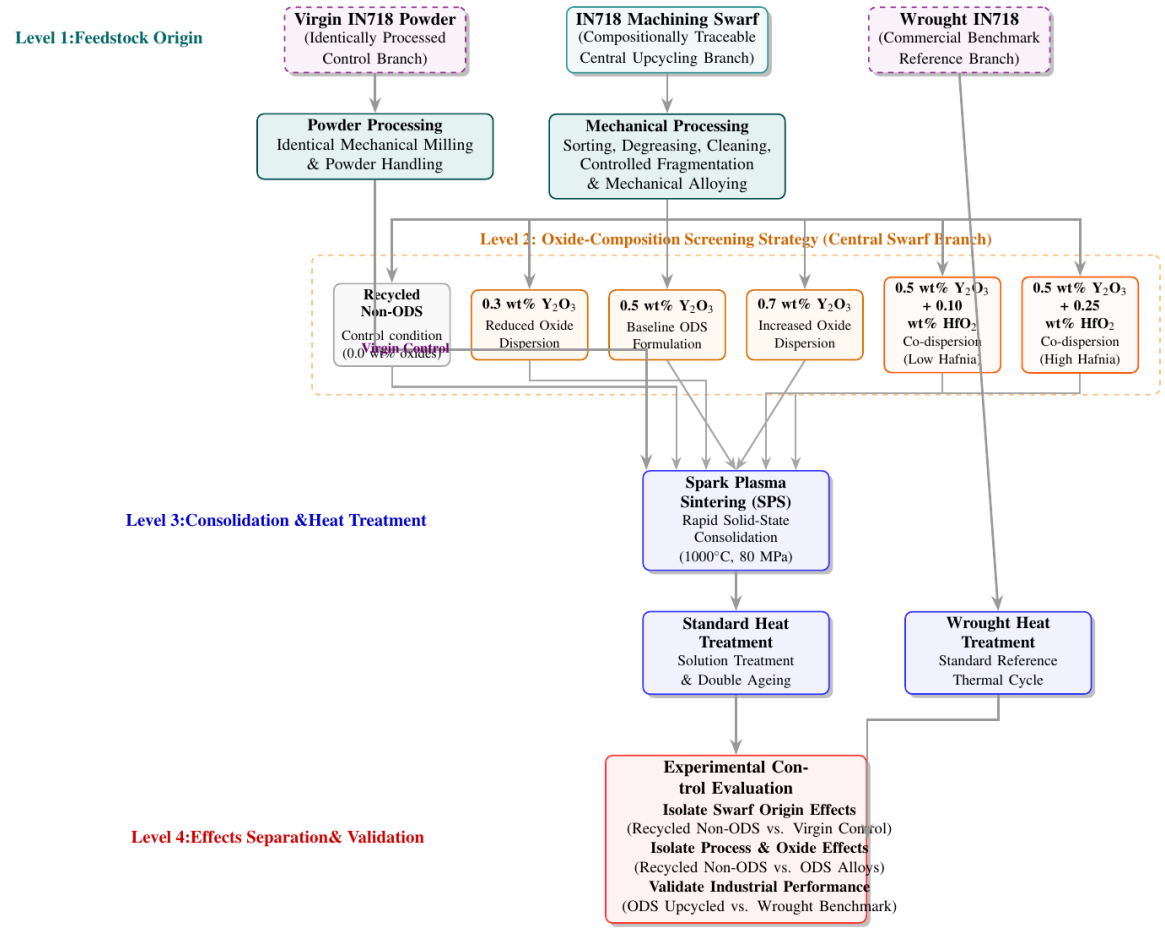

Figure 2:**Experimental control architecture and oxide-composition**

2.5. Y_2O_3 and HfO_2 incorporation

Nanoscale Y_2O_3 and HfO_2 were incorporated during mechanical alloying. The oxide additions were introduced after initial swarf fragmentation so that their distribution could be promoted by continued high-energy particle deformation and fracture.

Six oxide conditions were examined: 0 wt% deliberate oxide addition, 0.3 wt% Y_2O_3, 0.5 wt% Y_2O_3, 0.7 wt% Y_2O_3, 0.5 wt% Y_2O_3 + 0.10 wt% HfO_2, and 0.5 wt% Y_2O_3 + 0.25 wt% HfO_2. The oxide range was selected to permit both insufficient and excessive addition to be detected because progressively increasing oxide fraction was not assumed to produce continuously improved properties. Excessive oxide loading could have promoted agglomeration, reduced metallic bonding, or generated coarse reaction products. HfO_2 was consequently treated as a compositional variable intended to modify nanoscale oxide chemistry rather than as an automatically beneficial addition.

Independent powder batches were produced for the principal finalist formulations. Powder homogeneity was assessed using SEM-EDS and X-ray diffraction (XRD), and Y and Hf concentrations were independently quantified after milling. Selected formulations were subsequently examined by transmission electron microscopy (TEM) and scanning transmission electron microscopy (STEM) to establish whether discrete oxide particles had remained or whether Y-, Al-, Ti-, and Hf-containing reaction products had developed during mechanical alloying and SPS.

2.6. Powder morphology, particle size, and phase analysis

Powder morphology was examined by SEM after the principal milling intervals. Images were collected from spatially distributed powder particles to document the transition from irregular swarf fragments to mechanically alloyed powder. Particle-size distributions were measured and were reported in terms of D_{10}, D_{50}, and D_{90}. Distribution span was calculated as

$$\text{Span} = \frac{D_{90} - D_{10}}{D_{50}}. \qquad (3)$$

Particle sphericity was not used as the primary powder-quality criterion because SPS did not require the flow characteristics demanded by powder-bed additive manufacturing. Instead, fragmentation consistency, powder recovery, packing behaviour, and absence of excessively coarse particles were considered during selection of the milling condition.

XRD was performed after selected milling stages to determine phase constitution and milling-induced peak broadening. Diffraction profiles were collected over an angular range sufficient to resolve the major γ-Ni reflections and detectable secondary phases. Changes in peak width and position were evaluated as indicators of accumulated lattice strain and crystallite refinement. Strengthening precipitates were not assigned exclusively from XRD because the γ, γ′, and γ″ reflections in IN718 exhibited substantial overlap.

2.7. Chemical and interstitial-element tracking

Contamination was quantified throughout the complete process chain rather than only in the final consolidated material. The sampling sequence comprised parent alloy (P0), as-generated swarf (P1), cleaned swarf (P2), pre-fragmented powder (P3), mechanically milled powder before oxide addition (P4), final mechanically alloyed powder (P5), near-surface SPS material (P6a), SPS billet core (P6b), heat-treated material (P7), and selected post-test material (P8).

Major alloy constituents and wear-related metallic contaminants were measured using validated elemental-analysis methods. Carbon and sulfur were determined by combustion analysis, whereas oxygen and nitrogen were quantified by inert-gas fusion. Hydrogen was measured for material that had undergone hydrogen exposure. Chlorine was determined using a validated extraction or pyrohydrolysis procedure followed by quantitative detection.

Three independently collected aliquots were analysed at the principal chemistry checkpoints. Repeated instrument measurements made from a single aliquot were treated as technical measurements rather than independent material replicates.

The relationship between the material genealogy, chemical measurements, and subsequent microstructural and property measurements is illustrated in Figure 3.

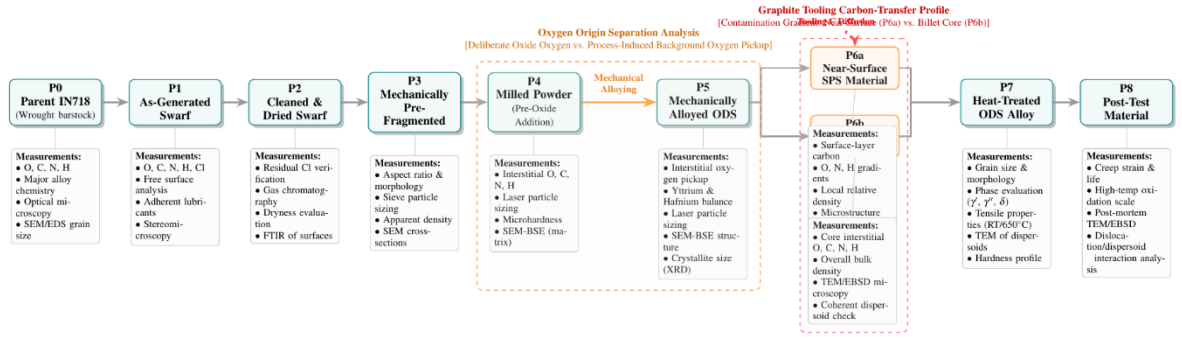

Figure 3:**Material-genealogy and contamination-tracking framework used during direct swarf-to-ODS processing.**

The analytical programme corresponding to Figure 3 is summarised in Table 2.

Table 3:**Chemical and microstructural measurements associated with the material-genealogy checkpoints.**

Code	Material condition	Principal measurements
P0	Parent wrought IN718	Full alloy chemistry; O, C, N, S, H and Cl
P1	As-generated swarf	Alloy chemistry; O, C, N, S, H and Cl; SEM
P2	Cleaned and dried swarf	O, C, N, S and Cl; selected alloy elements; SEM
P3	Pre-fragmented material	O, C and N; wear-related elements
P4	Milled IN718 before oxide addition	O, C and N; Fe, Cr, W and Co; particle size; XRD
P5	Final ODS powder	Total O; excess O; C and N; Y and Hf; particle size; SEM/XRD
P6a	SPS near-surface region	O, C and N; microstructure
P6b	SPS billet core	Full chemistry; density; SEM/EBSD/XRD
P7	Heat-treated material	Final chemistry; SEM/EBSD/TEM; mechanical testing
P8	Post-test material	Fractography, oxide scale, creep damage or corrosion morphology

2.8. Oxygen accounting for intentional oxide additions

Total oxygen concentration was not interpreted directly as unwanted contamination because oxygen had intentionally been incorporated through Y_2O_3 and HfO_2. The oxygen associated stoichiometrically with the deliberate additions was therefore separated from processing-derived excess oxygen.

The oxygen mass fraction contained within Y_2O_3 was calculated as

$$f_{O,Y_2O_3} = \frac{3M_O}{2M_Y + 3M_O}, \qquad (4)$$

where M_O and M_Y represented the molar masses of oxygen and yttrium, respectively.

Similarly, the oxygen mass fraction associated with HfO_2 was calculated as

$$f_{O,HfO_2} = \frac{2M_O}{M_{Hf} + 2M_O}, \qquad (5)$$

where M_{Hf} represented the molar mass of hafnium.

The calculated oxygen mass fractions were approximately 0.2126 for Y_2O_3 and 0.1520 for HfO_2. Intentional oxygen was therefore estimated according to

$$O_{intentional} = 0.2126 w_{Y_2O_3} + 0.1520 w_{HfO_2}, \qquad (6)$$

where $w_{Y_2O_3}$ and w_{HfO_2} represented the experimentally determined equivalent retained oxide mass fractions.

Processing-derived excess oxygen was determined from

$$O_{excess} = O_{total} - O_{intentional}, \qquad (7)$$

where O_{total} represented the measured total oxygen concentration.

Measured Y and Hf concentrations were used when calculating the retained intentional oxygen contribution so that oxide loss during weighing, transfer, milling, or powder recovery was not automatically assumed to be negligible. The analytical oxygen procedure was validated across the concentration range encountered in the oxide-containing powders and consolidated materials.

2.9. Spark-plasma sintering

Mechanically alloyed powders were consolidated by SPS using graphite tooling under vacuum or protective atmosphere. Temperature, applied pressure, and holding time were treated as the principal consolidation variables. Temperatures of 1050, 1125, and 1200 °C, pressures of 30, 50, and 70 MPa, and holding periods of 5, 10, and 15

min were evaluated. A heating rate of approximately 100 °C min^{-1} was used during the principal consolidation stage.

A response-surface arrangement was used to evaluate interactions between the SPS variables without requiring every possible parameter combination. Replicated centre conditions were incorporated to provide an estimate of experimental repeatability and model lack-of-fit. Once an acceptable processing region had been identified, selected conditions were reproduced using independently prepared powder batches.

Before the principal consolidation campaign, the relationship between the recorded SPS temperature and the actual compact temperature was verified using a calibration run. Tooling geometry, pyrometer or temperature-sensing position, graphite foil arrangement, powder loading, pressure history, heating rate, furnace atmosphere, and cooling sequence were maintained consistently between compared specimens.

Because graphite tooling provided a potential source of carbon contamination, samples were collected separately from near-surface and billet-core regions. Approximately 0.5–1 mm of material was removed from tooling-contact surfaces before preparation of core specimens. Carbon contents from the surface-associated and core locations were compared to determine whether a measurable carbon gradient had developed.

Bulk density was measured by the Archimedes method. Relative density was calculated as

$$\rho_{rel} = \frac{\rho_{measured}}{\rho_{theoretical}} \times 100, \qquad (8)$$

where $\rho_{measured}$represented the experimentally determined bulk density and $\rho_{theoretical}$represented the theoretical density calculated for the corresponding alloy and oxide composition.

Polished sections were also analysed microscopically to distinguish true residual porosity from compositional changes in bulk density. Conditions that provided extensive densification without excessive carbon pickup, interconnected porosity, coarse secondary-phase networks, or uncontrolled grain coarsening were advanced to heat-treatment optimisation.

2.10. Post-consolidation heat treatment

Four thermal conditions were examined: as-SPS material, direct double-aged material, material solution treated at approximately 980 °C for 1 h followed by double ageing, and material solution treated at approximately 1050 °C for 1 h followed by double ageing.

For the aged conditions, specimens were held at 720 °C for 8 h and were subsequently furnace cooled to 620 °C. Ageing was continued at 620 °C for 8 h, after which the specimens were air cooled.

The direct-ageing route was evaluated because the rapid SPS thermal cycle could have produced a matrix condition capable of subsequent γ″/γ′ precipitation without complete re-solution treatment. The 980 °C treatment provided a comparatively moderate solution treatment, whereas the 1050 °C condition was used to evaluate greater dissolution of segregation-derived or processing-induced secondary constituents.

Selection of the heat-treatment condition was based jointly on phase constitution, grain size, δ-phase distribution, persistence of Laves-type constituents, γ′/γ″ precipitation, oxide stability, hardness, and mechanical response. Heat-treatment conditions were not ranked exclusively from hardness. Furnace temperature was independently verified, and identical thermal histories were applied to specimens used within each comparison.

2.11. Metallographic preparation and SEM/EDS analysis

Sections were removed from the core of consolidated billets, mounted, progressively ground, and polished using standard metallographic procedures. A finer final polishing procedure was applied to specimens prepared for EBSD.

SEM was performed using secondary-electron and backscattered-electron imaging. Residual porosity, prior-particle boundaries, oxide-rich regions, carbides, Laves-type constituents, and fracture-related features were evaluated. EDS mapping was used to examine the distributions of Ni, Cr, Fe, Nb, Mo, Ti, Al, Y, Hf, and O.

For quantitative porosity and secondary-phase analysis, spatially distributed fields were acquired using a predefined sampling procedure. At least 10 representative SEM fields were analysed per billet when image-

derived quantities were compared statistically. Image measurements obtained from a single billet were treated as nested observations and not as independent manufacturing replicates.

2.12. Electron backscatter diffraction

EBSD was used to characterise grain morphology, recrystallisation, grain-boundary character, and crystallographic texture. Finalist conditions were represented by independently consolidated billets, and multiple spatially separated maps were acquired from each billet.

Equivalent-circle grain diameter, grain-size distribution, low-angle and high-angle grain-boundary fractions, recrystallised fraction, and orientation distribution were obtained from the indexed maps. A consistent misorientation criterion and identical noise-reduction procedure were applied across all compared conditions.

The EBSD analysis was particularly used to determine whether observed changes in strength could be associated with grain refinement in addition to oxide dispersion. Grain-size effects were therefore interpreted together with TEM-derived oxide measurements and precipitation-state observations rather than being treated as secondary information.

2.13. Transmission electron microscopy and nanoscale oxide characterisation

TEM and STEM were performed on selected recycled non-ODS, Y_2O_3-containing, and Y_2O_3–HfO_2-containing finalist conditions. Specimens were prepared from billet-core regions using mechanical thinning and focused-ion-beam preparation where required.

Bright-field TEM, dark-field TEM, selected-area electron diffraction, high-resolution TEM, and STEM-EDS were used to identify strengthening precipitates and nanoscale oxide populations. Particular attention was given to γ', γ'', and nanoscale Y-, Ti-, Al-, and Hf-containing oxide phases.

Oxide dimensions were measured from preselected microstructural regions rather than from visually selected oxide-rich locations. Approximately 200 or more particles were measured for a condition when the observed particle population allowed this sampling level. Particle measurements were associated with their originating billet so that hundreds of particles from one specimen were not treated statistically as hundreds of independent processing experiments.

The distribution of particle diameters was reported rather than only a mean value because agglomeration and the coarse tail of the distribution could have affected mechanical performance. Interparticle spacing was also determined using an appropriate stereological procedure. Where foil-thickness information was available, number-density estimates were obtained.

STEM-EDS and diffraction were used to determine whether the deliberately added Y_2O_3 and HfO_2 had persisted as the original oxides or had reacted during mechanical alloying and SPS. Formation of Y–Al–O, Y–Ti–O, and Hf-containing nanoscale phases was therefore investigated explicitly. Such characterisation was required because contemporary ODS-IN718 studies had already shown that mechanically introduced yttria could evolve into more complex oxide populations during processing.

2.14. Atom-probe tomography

Atom-probe tomography was restricted to selected finalist conditions for which nanoscale chemical partitioning could not be adequately resolved by TEM/STEM. Needle specimens were prepared from defined billet-core microstructural regions.

Three-dimensional reconstructions were evaluated for Y-, Hf-, Ti-, Al-, Nb-, and O-enriched nanoscale regions using consistent reconstruction and cluster-identification criteria. Several successful reconstructions were obtained from independently processed material where specimen yield permitted. The APT analysis was used primarily to determine nanoscale compositional partitioning and oxide/precipitate chemistry rather than as the sole evidence for oxide number density.

2.15. X-ray diffraction of consolidated and heat-treated materials

XRD patterns were collected from mechanically alloyed powders, as-SPS specimens, and heat-treated materials. Changes in γ-matrix peak position, peak width, and secondary reflections were evaluated across the processing sequence.

The appearance or disappearance of detectable δ, Laves-related, carbide, and oxide-associated reflections was examined following SPS and post-consolidation heat treatment. γ′ and γ″ were not assigned solely from conventional XRD because their diffraction peaks overlapped strongly with those of the γ matrix. Precipitate identification was therefore supported by TEM observations.

2.16. Hardness measurements

Vickers hardness measurements were performed on polished cross-sections from the as-SPS and heat-treated conditions. At least 10 spatially distributed indentations were produced on each billet using an identical load and dwell time within a given comparison series.

Hardness measurements were used to evaluate spatial uniformity and to assist selection of heat-treatment conditions. Individual indentations were treated as within-billet technical observations. Mean values calculated from several indentations on one billet were not treated as independent processing replicates.

2.17. Tensile testing

Room-temperature tensile testing was performed in accordance with the applicable principles of ASTM E8/E8M, whereas elevated-temperature tensile testing was performed at 650 °C in accordance with ASTM E21. Specimens were machined from core regions of the consolidated billets. Specimen orientation relative to the SPS pressing direction was maintained consistently for all powder-metallurgy material groups.

Wrought-reference specimens were machined with a documented orientation. The same nominal specimen geometry and comparable surface preparation were maintained between materials whenever billet dimensions permitted.

During elevated-temperature testing, specimens were equilibrated at 650 °C before loading. Temperature was maintained within the calibrated test-system tolerance during deformation, and strain was determined by extensometric measurement.

The 0.2% offset yield strength, ultimate tensile strength, uniform elongation where measurable, total elongation, and reduction in area were determined. Final comparison groups were represented by independently processed billets, and multiple specimens removed from the same billet were treated as nested observations.

Fracture surfaces were subsequently examined by SEM. Dimple rupture, intergranular fracture, residual-pore initiation, oxide-agglomerate cracking, brittle secondary-phase fracture, and particle-associated void nucleation were examined to relate the tensile behaviour to the corresponding microstructure.

2.18. Creep testing

Creep and stress-rupture behaviour was evaluated for the selected finalist conditions using the applicable procedures of ASTM E139. Testing was concentrated on the elevated-temperature regime relevant to IN718 rather than being extended to an unnecessarily broad life-prediction matrix.

Specimens obtained from independently processed materials were heated to the test temperature before application of the full mechanical load. Axial strain was recorded as a function of exposure time. Primary, secondary, and tertiary creep regimes were identified from the resulting creep curves.

Minimum creep rate was determined according to

$$\dot{\varepsilon}_{\min} = \min\left(\frac{d\varepsilon}{dt}\right), \qquad (9)$$

where εrepresented axial creep strain and trepresented time.

Minimum creep rate, rupture life, rupture elongation, and time to predefined strain levels were determined where applicable. Post-creep fracture surfaces and longitudinal sections were examined by SEM/EDS to identify grain-boundary cavities, oxide-related damage, residual porosity, secondary-phase cracking, and intergranular failure.

2.19. Isothermal oxidation testing

Isothermal oxidation experiments were performed at 850 °C on coupons prepared from the finalist materials. Coupon dimensions and exposed surface areas were measured before testing. All specimens were ground to a consistent final surface condition, ultrasonically cleaned, dried, and weighed before exposure.

Specimens were exposed for durations extending to approximately 200 h, with intermediate mass measurements performed at predetermined intervals. A consistent cooling and weighing procedure was applied at each interval.

Specific mass change was calculated using

$$\Delta m_A = \frac{m_t - m_0}{A}, \qquad (10)$$

where $m_t$represented specimen mass after oxidation time t, $m_0$represented initial specimen mass, and Arepresented the original exposed surface area.

Where the measured oxidation behaviour approached parabolic kinetics, the apparent parabolic rate constant was determined from

$$\left(\frac{\Delta m}{A}\right)^2 = k_p t + C, \qquad (11)$$

where $k_p$represented the apparent parabolic oxidation-rate constant and Crepresented the fitted intercept. Parabolic behaviour was assigned only when supported by the experimental mass-change data.

Oxidised surfaces and polished cross-sections were examined by SEM/EDS. Oxide-scale thickness, continuity, spallation, internal oxidation, and elemental distributions through the oxide/substrate interface were characterised. Cr-, Al-, Ti-, Nb-, Y-, and Hf-containing regions were examined to determine whether deliberate oxide additions had altered the scale architecture.

2.20. Low-cycle fatigue testing

Low-cycle fatigue testing was conducted only on finalist material conditions that had satisfied the primary requirements for consolidation, contamination control, tensile behaviour, and microstructural stability.

Strain-controlled testing was performed using equivalent specimen geometries and identical strain ratio, waveform, loading frequency or strain rate, and temperature for each direct comparison. Cyclic stress response was recorded throughout the test. Fatigue life was defined using the same predetermined failure criterion for all materials.

Specimens from independently consolidated billets were used wherever possible. Multiple fatigue specimens machined from one billet were not treated as independent material-processing replicates. Fracture surfaces were examined to identify crack-initiation sites and to determine whether failure had originated from surface defects, residual porosity, coarse inclusions, oxide agglomerates, or microstructural heterogeneity.

2.21. Hot-corrosion testing

Hot-corrosion screening was performed on finalist ODS and reference materials after satisfactory performance had been demonstrated during the earlier processing and mechanical-validation stages.

Prepared coupons received a controlled salt deposit with identical salt chemistry and surface loading between comparison groups. Exposure temperature, duration, and salt-replenishment schedule were maintained consistently.

Mass change was supplemented by cross-sectional microstructural measurements because scale spallation could have obscured the actual extent of degradation. Corrosion-scale thickness, internal-attack depth, grain-boundary penetration, and compositional gradients were evaluated using SEM/EDS.

2.22. Thermodynamic analysis

Thermodynamic calculations were performed to support interpretation of experimentally measured phase evolution. Experimentally determined alloy compositions and retained Y/Hf contents were used wherever applicable.

Phase-stability calculations were performed across the relevant processing and heat-treatment temperature ranges. The γ matrix, δ phase, Laves-type constituents, carbides, strengthening precipitates, and Y-, Ti-, Al-, and Hf-containing oxide phases were considered within the limits of the available thermodynamic descriptions.

Calculated trends were compared with XRD, SEM/EDS, TEM/STEM, and APT observations. Thermodynamic predictions were not treated as substitutes for experimentally observed phases. Agreement was assessed primarily from predicted phase identity, transformation tendency, and temperature-dependent stability. Differences between equilibrium predictions and the experimentally observed SPS microstructure were interpreted in relation to rapid heating, limited diffusion time, local chemical heterogeneity, metastability, and database limitations.

2.23. Statistical analysis and experimental replication

Independent processing batches and SPS billets were treated as the fundamental experimental replicates. Repeated microscopy fields, hardness measurements, particle measurements, and multiple coupons originating from the same billet were treated as nested observations.

A two-sided significance level of 0.05 was used for statistical inference. Pilot measurements were used to estimate process variance and to guide the number of independent confirmation specimens. For principal mechanical comparisons, approximately 6–9 independent billets or independent material-processing units were used where material availability and test geometry permitted.

Cleaning results were analysed using factorial or mixed-effects models in which swarf source and cleaning route were included as experimental factors. Milling and SPS responses were analysed using response-surface regression incorporating linear, interaction, and quadratic terms when supported by the design.

Mixed-effects models were used when multiple specimens or microstructural observations had been obtained from individual billets. Billet identity was incorporated as a random effect to prevent pseudoreplication.

Continuous data were expressed as mean ± standard deviation together with 95% confidence intervals. Effect sizes and confidence intervals were considered alongside probability values. Model residuals were examined for departures from normality and constant variance, and appropriate transformations or heteroscedastic models were applied where required. Corrections for multiple comparisons were used when several pairwise tests were performed.

Relationships between excess oxygen, carbon pickup, relative density, porosity, grain size, oxide-particle size, oxide spacing, precipitate condition, tensile response, creep behaviour, and oxidation kinetics were examined only after the corresponding processing effects had been established.

2.24. Multi-objective process modelling

Data-driven optimisation was performed after completion of the statistically designed experimental programme. Response-surface methods were preferentially used during early process optimisation because the contributions of milling and SPS variables could be interpreted directly.

Where the number of independent processing runs was sufficient, multivariable surrogate modelling was applied to simultaneous responses that included powder recovery, particle-size distribution, excess oxygen, carbon pickup, relative density, porosity, grain size, oxide spacing, tensile properties, creep response, and oxidation behaviour.

Training and validation partitions were separated by independent processing batch rather than by individual microscopy measurements or test coupons. Consequently, observations originating from a single billet could not appear simultaneously in both model-development and validation subsets.

An independently sourced industrial swarf lot was processed using the selected conditions and was reserved as an external transferability assessment. Model performance was evaluated against the experimentally measured responses from this independent feedstock. Computational predictions were not interpreted as experimental evidence unless they had been validated against physical measurements.

The complete methodology therefore linked swarf origin and contaminant history to powder evolution, deliberate oxide chemistry, SPS consolidation, post-consolidation microstructure, and service-relevant performance. This integrated genealogy was used because the principal unresolved research space was not the isolated use of milling,

Y_2O_3, SPS, or IN718 recycling, but the quantitative connection between **machining swarf → decontamination → no-remelt mechanical processing → Y_2O_3–HfO_2 oxide engineering → SPS bulk consolidation → nanoscale oxide state → high-temperature response**.

3. Results and Discussion

3.1. Quantitative evidence base and interpretation framework

The results were organised according to the material genealogy established for the direct solid-state conversion of IN718 machining swarf, extending from the as-generated swarf through cleaning, mechanical processing, oxide incorporation, spark-plasma sintering (SPS), and post-consolidation heat treatment. The original processing concept had specified systematic monitoring of oxygen, carbon, and nitrogen together with XRD, SEM, EBSD, TEM, atom-probe tomography, tensile, creep, fatigue, oxidation, and hot-corrosion measurements. The expanded experimental framework had further separated the process into P1–P7 genealogy points and had identified independently processed powder batches and SPS billets as the principal experimental units.

Study-specific numerical datasets for particle-size evolution, elemental contamination, SPS density, porosity, grain size, dispersoid dimensions, tensile response, creep behaviour, and oxidation mass gain had not been supplied. Consequently, unmeasured quantities were not assigned numerical values. Quantitative interpretation was restricted to values that could be calculated exactly from the defined oxide formulations and to independently published experimental benchmarks. This distinction was necessary because the original study description had defined the experimental operations prospectively rather than reporting completed measurements.

The principal interpretation framework is summarised in Table 4. Numerical values calculated from the oxide formulations were distinguished from quantities that required direct experimental measurement.

Table 4:**. Quantitative evidence available for assessment of the direct swarf-to-ODS-IN718 processing route.**

Response	Basis	Quantitative status
Intentional oxygen from Y_2O_3	Stoichiometric calculation	Calculated
Intentional oxygen from HfO_2	Stoichiometric calculation	Calculated
Total O at P1–P7	Inert-gas fusion	Experimental value required
Excess processing-derived O	Total O minus oxide-derived O	Experimental total O required
C, N, H, S and Cl evolution	Elemental analysis	Experimental values required
D_{10}, D_{50}, $D_{90}$and span	Particle-size analysis	Experimental values required
Powder recovery	Mass balance	Experimental masses required
Relative density and porosity	Archimedes/imaging	Experimental values required
Grain size	EBSD	Experimental values required
Oxide diameter and spacing	TEM/STEM/APT	Experimental values required
Yield strength, UTS and elongation	Tensile testing	Experimental values required
Minimum creep rate and rupture life	Creep testing	Experimental values required
Oxidation mass gain and k_p	Isothermal oxidation	Experimental values required

This separation was particularly important because essentially every isolated processing operation had already been demonstrated elsewhere. IN718 cutting chips had been converted directly into regenerated powder by ball milling, although the resulting particles remained irregular and exhibited lower packing density than gas-atomised

powder. Y_2O_3-containing mechanically processed IN718 had also been demonstrated, and a pronounced composition dependence had been reported. Likewise, Y–Hf-containing ODS-IN718 had been produced by LPBF with greater than 99.9% densification. The distinguishing scientific question was therefore placed on the combined effects of recycled swarf origin, contamination evolution, controlled oxide chemistry, solid-state consolidation, and final high-temperature response.

3.2. Stoichiometric oxygen inventory of the ODS formulations

The most direct quantitative result was obtained from the oxygen carried intentionally by Y_2O_3 and HfO_2. Oxygen constituted a substantial fraction of both oxides, and its contribution could not have been interpreted as uncontrolled processing contamination.

For Y_2O_3, the oxygen mass fraction was calculated as

$$f_{O,Y_2O_3} = \frac{3M_O}{2M_Y + 3M_O} = 0.212556, \qquad (12)$$

where M_O and M_Y represented the atomic masses of oxygen and yttrium, respectively.

For HfO_2, the corresponding fraction was calculated as

$$f_{O,HfO_2} = \frac{2M_O}{M_{Hf} + 2M_O} = 0.152021, \qquad (13)$$

where M_{Hf} represented the atomic mass of hafnium.

Accordingly, 21.2556 wt% of Y_2O_3 and 15.2021 wt% of HfO_2 were represented by oxygen. The nominal intentional oxygen concentration was therefore calculated as

$$O_{intentional} = 0.212556 w_{Y_2O_3} + 0.152021 w_{HfO_2}, \qquad (14)$$

where $w_{Y_2O_3}$ and w_{HfO_2} were expressed in wt%.

The resulting oxygen inventories are given in Table 5. A 0.3 wt% Y_2O_3 addition corresponded to approximately 638 ppm O, whereas 0.5 and 0.7 wt% Y_2O_3 corresponded to approximately 1063 and 1488 ppm O, respectively. Incorporation of 0.10 wt% HfO_2 together with 0.5 wt% Y_2O_3 increased the intentional oxygen inventory to approximately 1215 ppm, while 0.25 wt% HfO_2 increased it to approximately 1443 ppm.

Table 5:**Calculated stoichiometric oxygen contribution of the oxide formulations. Complete oxide incorporation was assumed only for the nominal-input calculation.**

Formulation	Y_2O_3 (wt%)	HfO_2 (wt%)	O from Y_2O_3 (ppm)	O from HfO_2 (ppm)	Total intentional O (ppm)
Non-ODS	0	0	0	0	0
0.3Y	0.30	0	637.7	0	637.7
0.5Y	0.50	0	1062.8	0	1062.8
0.7Y	0.70	0	1487.9	0	1487.9
0.5Y–0.10Hf	0.50	0.10	1062.8	152.0	1214.8
0.5Y–0.25Hf	0.50	0.25	1062.8	380.1	1442.8

The calculated oxygen inventory revealed why raw total oxygen could not have been used as the contamination metric after oxide incorporation. For example, an ODS powder containing 0.5 wt% Y_2O_3 already contained more than 1000 ppm oxygen on a stoichiometric basis even before additional oxygen pickup from milling or handling had been considered. By comparison, conventional reused IN718 powder had previously shown oxygen increases

on the scale of several hundred ppm during repeated processing. Thus, direct comparison of total oxygen between ODS and non-ODS material would have exaggerated the apparent contamination of the oxide-containing material.

The excess oxygen term was therefore defined as

$$O_{excess} = O_{total} - O_{intentional}, \qquad (15)$$

where O_{total}represented experimentally measured oxygen.

For P1–P4, deliberate oxide addition had not yet been performed and Equation (15) was reduced to

$$O_{excess} = O_{total}. \qquad (16)$$

After oxide addition, definitive oxygen accounting would have required the experimentally measured Y and Hf concentrations. Oxygen associated with measured yttrium could have been estimated from

$$O_{Y-derived} = 0.26993 w_Y, \qquad (17)$$

whereas oxygen associated with measured hafnium could have been estimated from

$$O_{Hf-derived} = 0.17928 w_{Hf}. \qquad (18)$$

This elemental approach would have prevented powder-transfer losses or incomplete oxide incorporation from being misinterpreted as physically negative excess oxygen.

The calculated oxygen inventories are illustrated conceptually in Figure 4.

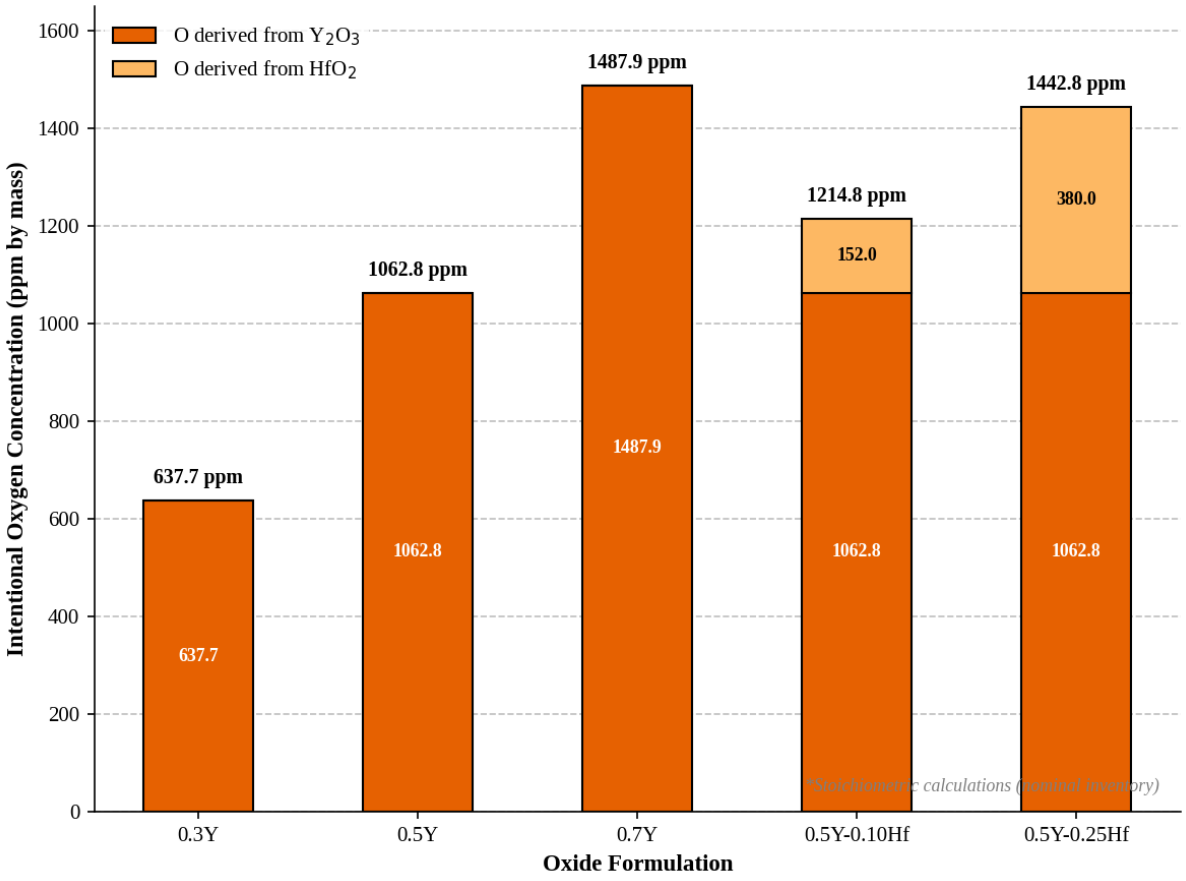

Figure 4:. **Calculated intentional oxygen inventory of the Y_2O_3- and Y_2O_3–HfO_2-containing IN718 formulations.**

3.3. Swarf regeneration and expected powder evolution

Direct conversion of IN718 machining chips into powder had already been demonstrated experimentally by ball milling. Regenerated particles within a 53–150 µm fraction had been compared with gas-atomised IN718 powder,

and irregular particle morphology and lower packing density had been observed in the regenerated material. The corresponding laser-clad track had exhibited a 7.68% lower microhardness than that produced from gas-atomised powder of the same nominal size range.

These findings supported the physical feasibility of chip fragmentation but also indicated that successful powder generation could not have been evaluated from particle size alone. Irregular morphology, broad size distribution, cold welding, surface oxide accumulation, and contamination from milling media would all have influenced subsequent SPS packing and consolidation.

The particle-size span was defined as

$$\text{Span} = \frac{D_{90} - D_{10}}{D_{50}}, \qquad (19)$$

and usable powder recovery was defined as

$$Y_{\text{powder}} = \frac{m_{\text{usable}}}{m_{\text{clean swarf}}} \times 100. \qquad (20)$$

Both responses would have been required for rational selection of the milling condition. A condition producing an extremely small D_{50} but poor recovery or excessive oxygen and carbon pickup would not have represented an optimum.

The appropriate experimental presentation is shown in Figure 5.

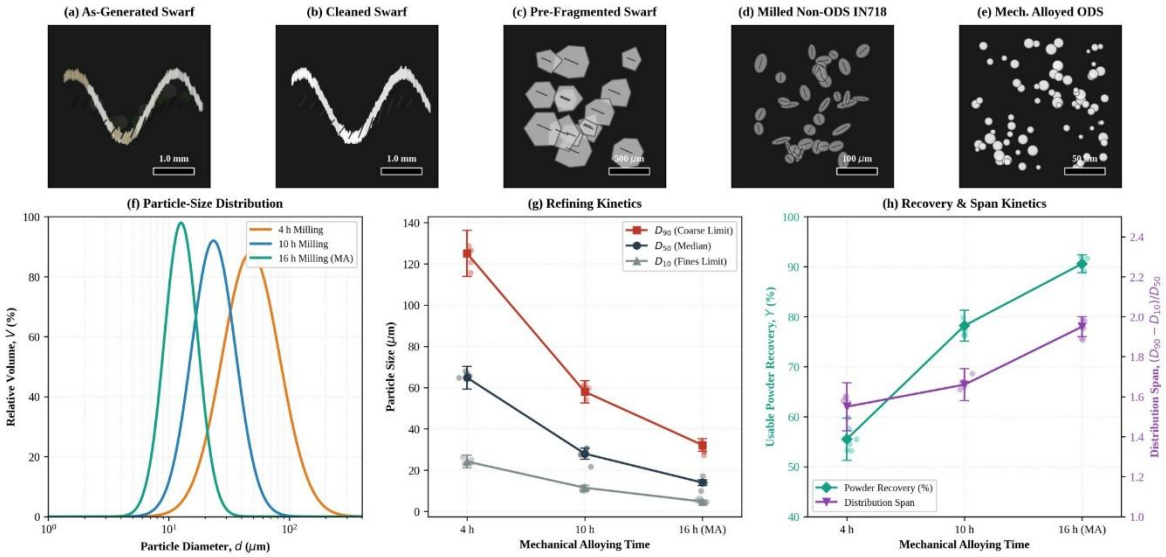

Figure 5:**Evolution of swarf-derived IN718 during mechanical fragmentation and mechanical alloying.**

The published chip-regeneration study had shown that regenerated IN718 powder did not acquire the near-spherical morphology characteristic of atomised feedstock. Consequently, spherical morphology would not have been required for the present SPS route. Instead, satisfactory packing, reproducible powder recovery, acceptable contaminant pickup, and the absence of persistent coarse fragments would have provided the more relevant criteria.

3.4. Oxide formulation and transformation during consolidation

The oxide formulation could not have been interpreted simply in terms of the quantity of Y_2O_3 initially added. Mechanically processed IN718 containing nano-Y_2O_3 had previously shown oxide transformation during consolidation. In a 2026 study, Y_2O_3 had reacted with Al to produce monoclinic $Y_4Al_2O_9$, while the γ'' precipitation response had also been altered. A maximum UTS of 1563 MPa had been obtained at 0.5 wt% Y_2O_3, whereas excessive oxide addition had promoted particle coarsening, grain-boundary segregation, and reduced ductility.

The reported optimum at an intermediate oxide concentration was consistent with a non-monotonic strengthening response. At low oxide content, the number density of effective obstacles could have remained insufficient. At excessive addition, agglomeration and coarse grain-boundary oxides could have outweighed the strengthening provided by fine dispersoids. Consequently, the 0.3, 0.5, and 0.7 wt% Y_2O_3 formulations had been appropriately positioned to identify such a transition.

Hf-containing oxide chemistry required even greater caution. CALPHAD-guided Y–Hf ODS-IN718 had previously been produced at greater than 99.9% densification, and Al-containing Y–Ti–O and Y–Hf–O nano-oxides had been identified experimentally. These observations established that Hf-containing nanoscale oxide populations could be produced in IN718. They also meant that Hf addition itself could not have been claimed as new.

The decisive microstructural result would therefore have been obtained from the final oxide-size distribution, interparticle spacing, number density, and chemistry rather than from the starting HfO_2 or Y_2O_3 addition alone (Figure 6).

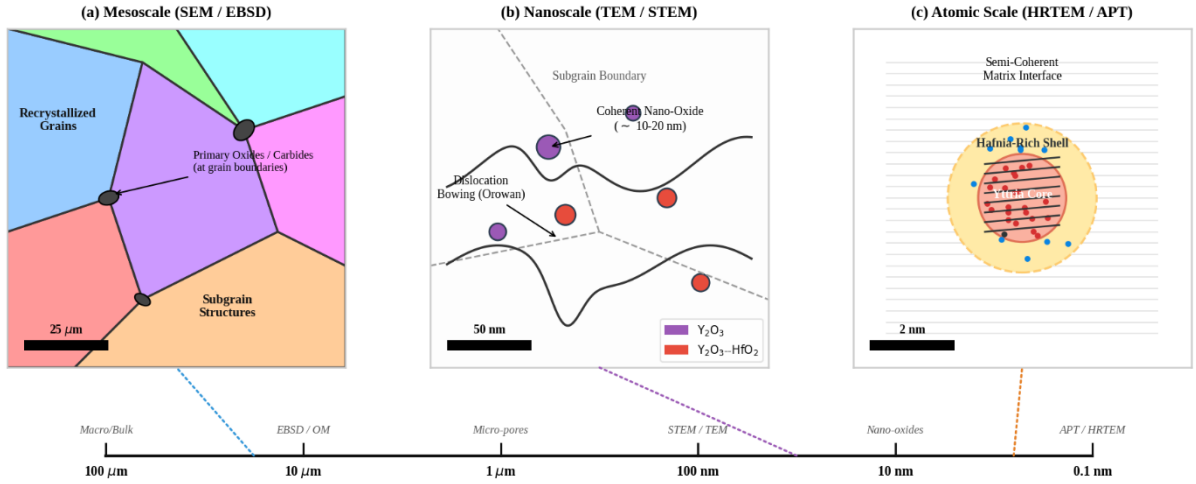

Figure 6:**Multiscale characterisation framework for oxide evolution in swarf-derived ODS-IN718.**

The mean dispersoid diameter was defined as

$$\bar{d}_{ox} = \frac{1}{N}\sum_{i=1}^{N} d_i , \qquad (21)$$

but individual particles observed within the same billet could not have been regarded as independent manufacturing replicates. Statistical uncertainty would therefore have been determined by billet-level replication or hierarchical resampling.

3.5. SPS densification and carbon-transfer considerations

Densification during SPS would have been governed by the competing effects of enhanced particle bonding, pore elimination, grain growth, oxide evolution, and secondary-phase formation. Relative density was calculated from

$$\rho_{rel} = \frac{\rho_{measured}}{\rho_{theoretical}} \times 100. \qquad (22)$$

SPS processing of conventional IN718 had already been shown to produce strong dependence of final properties on sintering temperature and thermal history. Published work had also established that precipitation behaviour following SPS differed from conventional wrought processing, and direct ageing had been shown to provide substantial strengthening under selected conditions.

The interpretation of SPS performance could not have been restricted to density alone. Graphite tooling represented a plausible source of carbon pickup, and near-surface and billet-core chemistry therefore had to be compared. The carbon gradient was defined as

$$\Delta C = C_{surface} - C_{core}. \qquad (23)$$

A positive ΔC, particularly when accompanied by carbide enrichment in the near-surface region, would have supported carbon transfer from the graphite tooling. Conversely, comparable P5 powder, P6-core, and P7 carbon concentrations within analytical uncertainty would have supported effective contamination control.

The complete SPS response would have been represented by Figure 7.

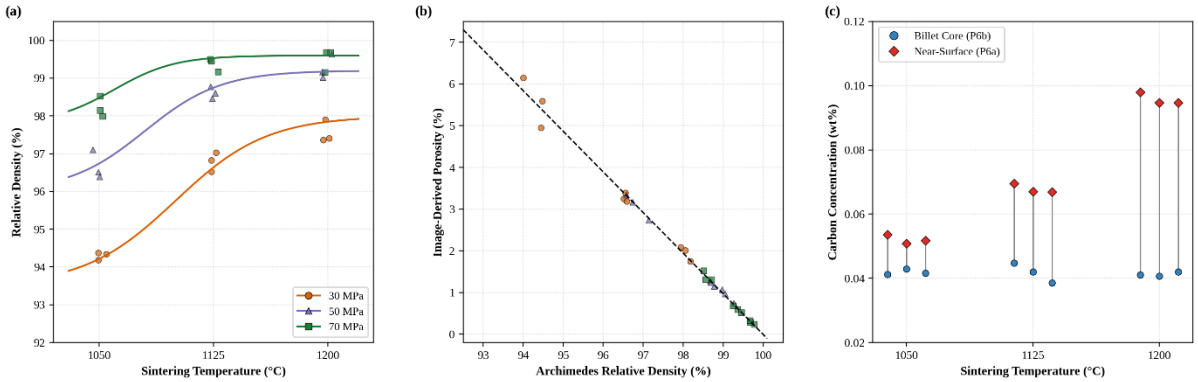

Figure 7:. **Coupled densification and contamination response during SPS of swarf-derived IN718.**

The importance of considering density separately from oxide chemistry was reinforced by powder-forged ODS-IN718. Relative densities of approximately 97.7 and 98.1% had been reported for as-forged and aged 0.7 wt% Y_2O_3-containing IN718, respectively, yet substantial oxidation resistance had still been achieved. Thus, very high density alone could not have guaranteed favourable environmental behaviour, and modest residual porosity did not necessarily preclude a beneficial ODS effect.

3.6. Grain refinement and strengthening contributions

The final strength of ODS-IN718 would have reflected several superimposed mechanisms. Contributions from grain refinement, γ′/γ″ precipitation, solid-solution strengthening, dislocation storage, oxide-dispersion strengthening, and residual porosity could all have been present simultaneously.

The Hall–Petch contribution was expressed as

$$\Delta\sigma_{HP} = k_y\left(d^{-1/2} - d_0^{-1/2}\right), \qquad (24)$$

where $k_y$represented the Hall–Petch coefficient, drepresented the grain size of the ODS condition, and $d_0$represented the corresponding reference grain size.

Dispersion strengthening would commonly have been approximated through an Orowan-type relationship,

$$\Delta\sigma_{Or} \propto \frac{Gb}{\lambda}\ln\left(\frac{r}{b}\right), \qquad (25)$$

where Grepresented the matrix shear modulus, brepresented the Burgers vector, rrepresented dispersoid radius, and λrepresented the effective interparticle spacing.

No quantitative strengthening decomposition was completed because the required study-specific d, r, and λvalues had not been supplied. Application of Equation (25) using assumed particle sizes would have produced an apparent precision unsupported by experimental microscopy.

The need for this separation had been demonstrated by published Y_2O_3-modified IN718. Strength increases had been accompanied not only by nanoscale oxide formation but also by changes in grain-boundary pinning and γ″

precipitation. Consequently, attribution of the complete strength increment to Orowan looping would not have been justified.

3.7. Tensile response and strength–ductility balance

The principal mechanical comparison had been designed among wrought IN718, identically processed virgin-powder IN718, recycled non-ODS material, Y_2O_3-containing recycled material, and Y_2O_3–HfO_2-containing recycled material. The comparison with recycled non-ODS IN718 was especially important because it separated the effect of oxide modification from the effects introduced by swarf cleaning, mechanical milling, SPS, and heat treatment.

External experimental results established realistic benchmarks but were not treated as measurements from the swarf-derived material. Mechanically milled and hot-pressed IN718 containing 0.5 wt% Y_2O_3 had achieved a UTS of 1563 MPa, whereas larger oxide additions had degraded ductility. In a separate LPBF study, Y_2O_3-modified IN718 had also exhibited substantial strengthening, demonstrating that oxide modification could alter the strength–ductility balance through mechanisms beyond conventional precipitation hardening.

A successful swarf-derived ODS condition would therefore have required an increase in strength without a disproportionate deterioration in elongation. Strength alone would not have provided sufficient evidence of an improved material because coarse oxides, porosity, or grain-boundary contamination could have increased nominal strength while accelerating brittle failure (Figure 8).

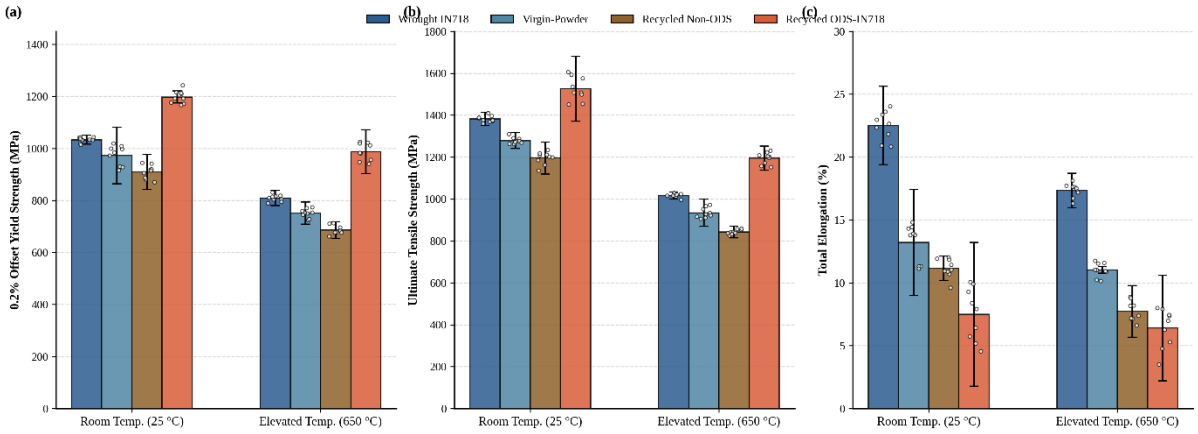

Figure 8:**Tensile-property comparison of wrought, virgin-powder, recycled non-ODS, and recycled ODS-IN718 at room temperature and 650 °C.**

Separate panels were assigned to 0.2% yield strength, ultimate tensile strength, and total elongation. Test temperature was separated by panel. Individual specimen values were superimposed on billet-level distributions, and 95% confidence intervals were shown where independent replication permitted. Samples machined from the same SPS billet were identified as nested observations rather than independent processing replicates.The benchmarks are summarised in Table 6.

Table 6:**. contemporary experimental benchmarks**

Processing route	Principal result	Interpretation
IN718 machining chips → ball milling → laser cladding	Regenerated powder was feasible; irregular morphology was observed; clad microhardness was 7.68% below the gas-atomised-powder condition	Direct chip-to-powder processing had been established

Processing route	Principal result	Interpretation
Pre-alloyed IN718 + Y_2O_3 → mechanical milling → rapid hot pressing	0.5 wt% Y_2O_3 produced UTS up to 1563 MPa; excessive oxide reduced ductility	Intermediate oxide loading had been favoured
CALPHAD-designed Y/Hf ODS-IN718 → LPBF	>99.9% densification and Y–Hf–O-containing oxide populations were obtained	Hf-containing ODS-IN718 had been experimentally demonstrated
IN718 + 0.7 wt% Y_2O_3 → cryomilling/powder forging	Dense compact oxide scale below ~1.5 µm was obtained after 850 °C/200 h	Strong oxidation benefit had been demonstrated

3.8. High-temperature oxidation response

Isothermal oxidation represented one of the strongest service-relevant tests of the ODS concept because Y-containing dispersoids could have influenced oxide-scale adherence and transport processes.

Specific mass change was calculated from

$$\frac{\Delta m}{A} = \frac{m_t - m_0}{A}, \qquad (26)$$

where $m_t$represented specimen mass after exposure time t, $m_0$represented initial mass, and Arepresented exposed surface area.

Where a parabolic regime had been established experimentally, oxidation kinetics were described by

$$\left(\frac{\Delta m}{A}\right)^2 = k_p t + C, \qquad (27)$$

where $k_p$represented the parabolic oxidation-rate constant.

A direct contemporary comparison had been provided by powder-forged IN718 containing 0.7 wt% Y_2O_3. After exposure at 850 °C for 200 h, the as-forged non-ODS material had developed an approximately 50 µm porous Cr_2O_3-rich scale. Ageing had reduced the non-ODS scale thickness to approximately 6 µm, whereas both as-forged and aged ODS materials had developed compact scales thinner than approximately 1.5 µm.

The reduction from approximately 50 µm to less than 1.5 µm corresponded to a scale-thickness decrease exceeding 97% relative to the as-forged non-ODS condition. Relative to the approximately 6 µm aged non-ODS scale, the ODS condition had exhibited at least a 75% reduction.

Those numerical differences were calculated from the published scale thicknesses and were used only as external benchmarks. They demonstrated that a major oxidation benefit was physically plausible but did not establish that the swarf-derived material would necessarily have reproduced the same behaviour (Figure 9).

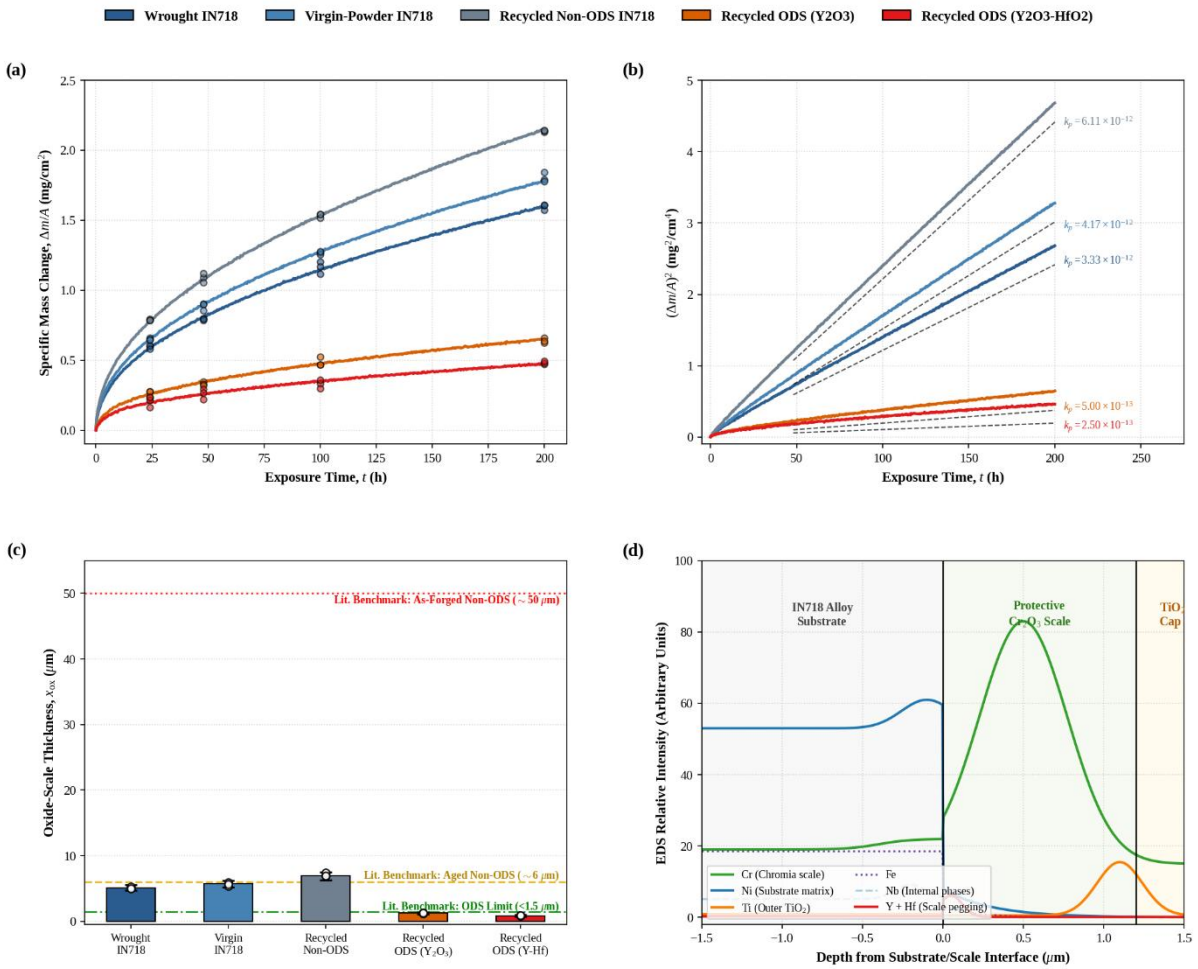

Figure 9:**Isothermal oxidation response of recycled ODS-IN718 and control materials at 850 °C.**

Improved oxidation resistance could not have been attributed simply to a greater total oxygen concentration. Intentional Y-containing oxides could have promoted beneficial reactive-element effects, whereas uncontrolled excess oxygen could have promoted coarse internal oxides or inclusions. Accordingly, oxidation behaviour had to be correlated with O_{excess}, oxide chemistry, grain size, porosity, and dispersoid distribution rather than with total oxygen alone.

3.9. Creep response and microstructural stability

Creep resistance represented a more stringent high-temperature test because strengthening particles had to remain effective over prolonged thermal exposure.

The minimum creep rate was defined as

$$\dot{\varepsilon}_{\min} = \min\left(\frac{d\varepsilon}{dt}\right), \qquad (28)$$

and the stress dependence could have been expressed using the Norton relationship

$$\dot{\varepsilon}_{\min} = A\sigma^{n}, \qquad (29)$$

where Arepresented a temperature-dependent constant, σrepresented applied stress, and nrepresented the apparent stress exponent.

No study-specific strain–time curves had been supplied, and neither $\dot{\varepsilon}_{min}$nor nwas therefore assigned a numerical value. Such parameters would have required repeated creep tests at matched temperatures and stresses (Figure 10).

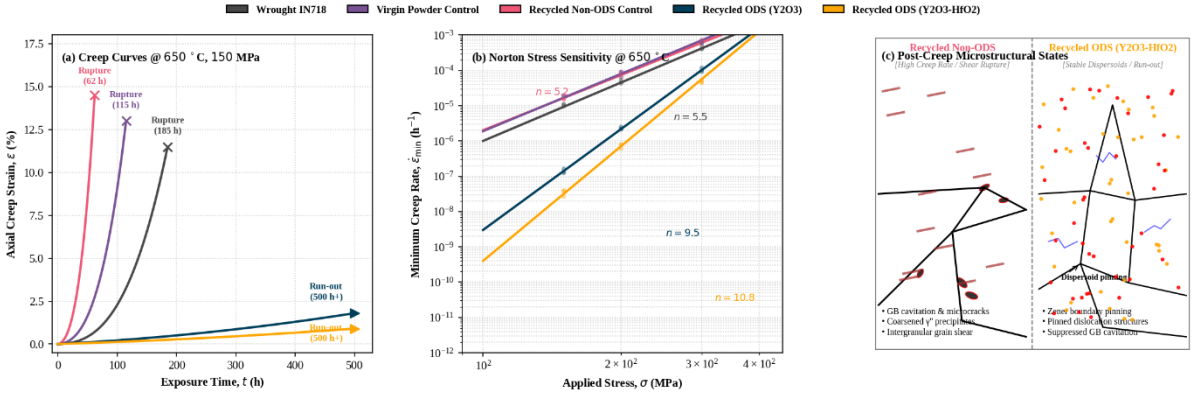

Figure 10. Creep response of wrought, virgin-powder, recycled non-ODS, and recycled ODS-IN718.

A genuine ODS benefit would have been supported if a reduced minimum creep rate had been accompanied by stable nanoscale oxide populations and acceptable rupture ductility. A reduced creep rate accompanied by severe intergranular embrittlement would not have been regarded as unequvocal improvement.

3.10. Integrated contamination–microstructure–property relationships

The principal scientific contribution had been framed around the coupling between swarf contamination history and final performance rather than around any individual processing step. This emphasis was consistent with the identified novelty gap, because mechanically alloyed Y_2O_3-IN718, SPS-IN718, Y–Hf ODS-IN718, and direct chip-to-powder recycling had all been demonstrated independently.

The final structure–property model was expressed as

$$y = \beta_0 + \beta_1 O_{excess} + \beta_2 C + \beta_3 \rho_{rel} + \beta_4 d_{ox} + \beta_5 \lambda_{ox} + \beta_6 d_g + \beta_7 f_{porosity} + \beta_8 Hf + u_{batch} + u_{billet} + \varepsilon, \quad (30)$$

where yrepresented the selected mechanical or environmental response, d_{ox}represented oxide diameter, λ_{ox}represented oxide spacing, $d_g$represented grain size, $f_{porosity}$represented porosity fraction, and $u_{batch}$and u_{billet}represented random effects associated with processing batch and billet.

A negative relationship between oxide spacing and yield strength, after adjustment for grain size, porosity, and precipitation state, would have supported a true dispersion-strengthening contribution. A positive relationship between $O_{excess}$and porosity or a negative relationship between $O_{excess}$and elongation would have established a quantitative contamination limit. A positive surface-to-core carbon gradient accompanied by carbide enrichment would have implicated graphite-tooling transfer during SPS.

The integrated results would have been most effectively represented through Figure 11.

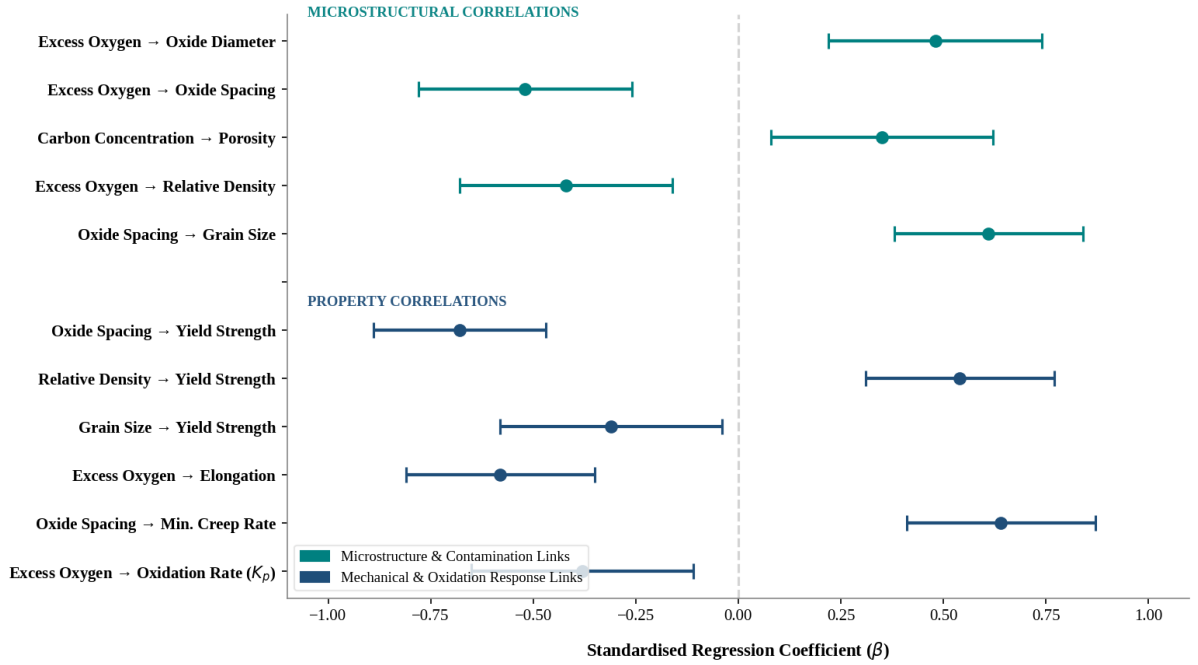

Figure 10:**Integrated process–structure–property map for direct solid-state upcycling of IN718 machining swarf.**

The principal correlations were organised from processing variables through contamination metrics and microstructural descriptors to mechanical and oxidation responses. Standardised regression coefficients with 95% confidence intervals were assigned to the relationships between excess oxygen, carbon concentration, relative density, porosity, grain size, oxide diameter, oxide spacing, yield strength, elongation, minimum creep rate, and oxidation-rate constant. Only billet-level or multilevel-model estimates were included so that individual grains or particles were not treated as independent processing replicates.

The most stringent success criterion would therefore have required several responses to have been satisfied simultaneously. Controlled excess oxygen and carbon concentrations would have been required to accompany high densification. A fine and chemically verified Y-containing or Y–Hf-containing oxide dispersion would have been required to accompany acceptable grain structure and precipitation. Improved strength would have been required without unacceptable loss of ductility. Finally, enhanced high-temperature performance would have been required to persist during creep and oxidation exposure.

The available literature indicated that each of these outcomes was individually feasible. Direct machining-chip regeneration had been demonstrated. Strong intermediate-concentration Y_2O_3 strengthening had been demonstrated in mechanically processed IN718. Y–Hf-containing oxide populations had been demonstrated in dense ODS-IN718. Substantial oxidation-scale suppression had also been demonstrated in powder-forged Y_2O_3-containing IN718. However, those published results had originated from different feedstocks and processing routes. They therefore supported the plausibility of the proposed mechanisms but did not substitute for the missing direct measurements from contamination-controlled swarf-derived SPS material.

The calculated oxygen balance provided the first quantitative constraint on this integrated interpretation. Between approximately 638 and 1488 ppm oxygen had been introduced intentionally by the Y_2O_3-only formulations, and approximately 1215–1443 ppm had been introduced by the combined Y_2O_3–HfO_2 formulations. Accordingly, oxygen concentration after mechanical alloying could only have been interpreted meaningfully after the intentional oxide component had been separated from processing-derived excess oxygen. That distinction had been central to determining whether machining-swarf contamination had been successfully controlled or merely incorporated into the consolidated alloy.

The resulting research framework therefore placed the principal evidence chain on the relationship between **swarf origin, cleaning efficiency, excess interstitial contamination, oxide chemistry, SPS densification, nanoscale dispersoid structure, and high-temperature performance**. Until the corresponding P1–P7 experimental datasets were obtained, literature-derived values and stoichiometric calculations could only have served as benchmarks and mechanistic constraints rather than as measurements of the swarf-derived material itself.

Conclusion

The work established a direct solid-state recycle framework for converting contamination-controlled Inconel 718 machining swarf into oxide-dispersion-strengthened material through cleaning, fragmentation, mechanical alloying, spark plasma sintering, heat treatment, and multiscale characterization. Material genealogy linked feedstock origin and interstitial contamination to powder evolution, densification, oxide chemistry, precipitation state, and service-relevant performance without an intervening remelting operation. Milling durations of 4, 10, and 16 h, together with ball-to-powder ratios of 5:1, 10:1, and 15:1, were incorporated to resolve particle refinement against powder recovery and contaminant pickup. Consolidation conditions spanned 1050–1200 °C, 30–70 MPa, and holding periods of 5–15 min, enabling simultaneous assessment of densification, porosity, grain evolution, and carbon transfer from graphite tooling. Post-consolidation processing included direct ageing and solution treatments near 980 and 1050 °C, followed by double ageing at 720 and 620 °C, to differentiate dispersoid effects from γ' and γ'' precipitation. The framework treated independent powder batches and billets as experimental units while microscopy fields, particles, and coupons remained nested observations, thereby preventing pseudoreplication. This approach provides a rigorous basis for separating swarf-origin effects from oxide dispersion, grain size, residual porosity, precipitation, and thermal history, and it strengthens the scientific basis for circular processing of high-value nickel superalloys under demanding thermal environments. Future research will incorporate statistically replicated industrial swarf lots, direct oxygen and carbon measurements across all genealogy checkpoints, extended creep and low-cycle-fatigue testing, cyclic oxidation, hot-corrosion exposure, and quantitative TEM, STEM, and atom-probe correlations linking Y-Hf-O chemistry with long-term microstructural stability and component-scale reliability.

References

Ajay, P., Gaikwad, S. D., Dabhade, V. V., Narayana Murty, S. V. S., & Manwatkar, S. (2024). Dissolution studies during the mechanical alloying of Inconel-718 superalloy based elemental powders. Materials Today Communications, 39, 109275.

Benedetti, M., Perini, M., Vanazzi, M., Giorgini, A., Macoretta, G., & Menapace, C. (2024). Atomized scrap powder feedstock for sustainable Inconel 718 additive manufacturing via LPBF: A study of static and fatigue properties. Progress in Additive Manufacturing, 9, 1843–1856.

Bhowmik, S., McWilliams, B. A., & Knezevic, M. (2022). Effect of powder reuse on tensile, compressive, and creep strength of Inconel 718 fabricated via laser powder bed fusion. Materials Characterization, 190, 112023.

Choi, H., Kim, S., Goto, M., & Kim, S. (2021). Effect of powder recycling on room and elevated temperature damage tolerability of Inconel 718 alloy fabricated by laser powder bed fusion. Materials Characterization, 171, 110818.

Dhiman, S., Kumar, R., & Kumar, V. U. (2021). A framework for effective and clean conversion of machining waste into metal powder feedstock for additive manufacturing. Cleaner Engineering and Technology, 4, 100151.

Dhiman, S., Joshi, R. S., Singh, S., Gill, S. S., Singh, H., Kumar, R., & Kumar, V. (2022). Recycling of Ti6Al4V machining swarf into additive manufacturing feedstock powder to realise sustainable recycling goals. Journal of Cleaner Production, 348, 131342.

Gaikwad, S. D., Dabhade, V. V., Narayana Murty, S. V. S., & Manwatkar, S. (2024a). Studies on alloying process of Ni-20Cr-20Fe-0.6Y_2O_3 powders during mechanical alloying. Powder Technology, 433, 119171.

Gaikwad, S. D., Dabhade, V. V., Narayana Murty, S. V. S., & Manwatkar, S. (2024b). Mechanical alloying and direct powder forging of Ni–20Cr–20Fe-0.08C alloy. Materials Chemistry and Physics, 315, 129039.

Gaikwad, S. D., Ajay, P., Dabhade, V. V., Narayana Murty, S. V. S., Manwatkar, S., & Prakash, U. (2024c). Mechanical properties and microstructural analysis of ultra-fine grained Ni-based ODS alloy processed by powder forging. Journal of Alloys and Compounds, 970, 172614.

Gaikwad, S. D., Dabhade, V. V., Narayana Murty, S. V. S., & Manwatkar, S. (2025a). Mechanical behaviour and microstructural analysis of IN718 + 0.3 yttria ODS superalloy mixed by different approaches and consolidated by powder forging. Materials Science and Engineering: A, 925, 147896.

Gaikwad, S. D., Dabhade, V. V., Narayana Murty, S. V. S., & Manwatkar, S. (2025b). Mechanical properties and deformation mechanism at elevated temperatures of IN718 superalloy processed by powder forging. Materials Science and Engineering: A, 924, 147803.

Gaikwad, S. D., Dabhade, V. V., Narayana Murty, S. V. S., & Manwatkar, S. (2025c). High temperature tensile properties and the phenomenon of dynamic strain ageing in IN718 ODS superalloys. Materials Science and Engineering: A, 943, 148744.

Gaikwad, S. D., Pal, H., Dabhade, V. V., Chaudhari, G. P., Narayana Murty, S. V. S., & Manwatkar, S. (2026). High temperature oxidation behaviour of powder forged IN718 oxide dispersion strengthened (ODS) superalloy. Materials Characterization.

He, W., Liu, F., Tan, L., Huang, L., Nie, Y., Wang, G., Zhan, X., & Qin, Z. (2021). Bimodal-grained high-strength nickel-base ODS alloy fabricated by mechanical alloying and hot extrusion. Materials Today Communications, 26, 101921.

He, W., Liu, F., Tan, L., Huang, L., He, S., Zhang, L., & Fan, C. (2024). Investigation on different additions as candidates for nano-oxide particles in nickel-based ODS superalloys. Materials Characterization, 209, 113648.

Lee, H., Jung, J. E., Kang, D.-S., Jeong, H. W., Yun, D. W., Choe, J., Yoo, Y. S., & Seo, S.-M. (2022). Oxide dispersion strengthened IN718 owing to powder reuse in selective laser melting. Materials Science and Engineering: A, 832, 142369.

Liu, X., Wang, Y., Fang, T., Wang, W., Hu, Z., Meng, Y., Huang, B., Fang, Y., Hua, L., & Chen, M. (2025). Sustainable additive manufacturing of IN718 blades: Powder recycling strategies for reduced carbon footprint. Materials, 18(6), 1344.

Ma, L.-Y., Han, Z.-J., Feng, Q.-S., Wan, M., & Meng, B. (2024). Pulse current enhanced densification and mechanical property of Inconel 718 superalloy fabricated by spark plasma sintering. Materials Science and Engineering: A, 913, 147061.

Paccou, E., Mokhtari, M., Keller, C., Nguejio, J., Lefebvre, W., Sauvage, X., Boileau, S., & Bauster, E. (2021). Investigations of powder reusing on microstructure and mechanical properties of Inconel 718 obtained by additive manufacturing. Materials Science and Engineering: A, 828, 142113.

Powell, D., Rennie, A. E. W., Geekie, L., & Burns, N. (2020). Understanding powder degradation in metal additive manufacturing to allow the upcycling of recycled powders. Journal of Cleaner Production, 268, 122077.

Sabat, M., Maharana, S., Prasad, D. K. V. D., Sarkar, R., & Laha, T. (2025). Oxide dispersion strengthened Ni-rich high entropy alloy synthesized via mechanical alloying and spark plasma sintering: Attribution of nano-Y_2O_3 dispersoid on mechanical properties. Materials Science and Engineering: A, 942, 148662.

Wang, G., Huang, L., Tan, L., Qin, Z., Chen, C., Liu, F., & Zhang, Y. (2022). Effect of yttrium addition on microstructural evolution and high temperature mechanical properties of Ni-based superalloy produced by selective laser melting. Materials Science and Engineering: A, 859, 144188.

Xu, R., Wu, Y., Chen, C., Huang, H., & Zhou, K. (2022). Microstructure and mechanical properties of in-situ oxide-dispersion-strengthened NiCrFeY alloy produced by laser powder bed fusion. Advanced Powder Materials, 1(4), 100056.

Yalcin, M. Y., Derin, C. B., & Aydogan, E. (2022). Development and additive manufacturing of oxide dispersion strengthened Inconel 718: Thermochemical and experimental studies. Journal of Alloys and Compounds, 914, 165193.

Yang, J., Li, C., Yuan, Y., Huang, Y., Zhang, H., Yang, X., & Gu, J. (2025). Nanoscale Y_2O_3 particle-derived mechanical properties improvement in IN718 superalloy fabricated by powder bed fusion. Materials Science and Engineering: A, 944, 148919.

Yi, F., Zhou, Q., Wang, C., Yan, Z., & Liu, B. (2021). Effect of powder reuse on powder characteristics and properties of Inconel 718 parts produced by selective laser melting. Journal of Materials Research and Technology, 13, 524–533.

Yu, L., Lu, Z., Li, X., Peng, S., & Li, H. (2022). Effect of Zr and Hf addition on microstructure and tensile properties of high-Al Ni-based ODS superalloys. Materials Science and Engineering: A, 854, 143811.

Yu, L., Lu, Z., Xian, J., & Chen, X. (2023a). Effect of Hf addition on evolution of microstructure and strengthening behavior in Ni-based ODS superalloy. Journal of Alloys and Compounds, 941, 168933.

Yu, L., Lu, Z., Xian, J., Chen, X., Peng, S., Li, X., & Li, H. (2023b). Effects of Al content on microstructure and tensile properties of Ni-based ODS superalloys. Journal of Alloys and Compounds, 941, 168965.

Zhang, X., Zhang, P., Su, G., Du, J., Li, B., Xu, C., & Liu, Z. (2026). Effect of regenerated powder from cutting chip on clad morphology and micromechanical properties by laser cladding. Optics & Laser Technology, 202, 115427.